

Rheological evolution of a trachybasalt from Mt. Etna under slow cooling

Received: 18 December 2025

Accepted: 9 March 2026

Cite this article as: Di Fiore, F., Vona, A. Rheological evolution of a trachybasalt from Mt. Etna under slow cooling. *Sci Data* (2026). <https://doi.org/10.1038/s41597-026-07048-y>

Fabrizio Di Fiore & Alessandro Vona

We are providing an unedited version of this manuscript to give early access to its findings. Before final publication, the manuscript will undergo further editing. Please note there may be errors present which affect the content, and all legal disclaimers apply.

If this paper is publishing under a Transparent Peer Review model then Peer Review reports will publish with the final article.

Rheological evolution of a trachybasalt from Mt. Etna under slow coolingFabrizio Di Fiore^{1,*} and Alessandro Vona²

¹ Istituto Nazionale di Geofisica e Vulcanologia, Sezione di Roma 1, Via di Vigna Murata 605, 00143 Roma, Italy

² Dipartimento di Scienze, Università degli Studi Roma Tre, L.go San Leonardo Murialdo 1, 00146 Roma, Italy

***Corresponding author**

Fabrizio Di Fiore

Istituto Nazionale di Geofisica e Vulcanologia,

Via di Vigna Murata 605, 00143 Rome, Italy

Email: fabrizio.difiore@ingv.it

Abstract

Understanding the rheological evolution of solidifying magma during its migration through the crust and the subsequent emplacement as lava is critical for assessing volcanic hazards. Crystallization plays a primary role in governing the rheology of low-viscosity basaltic magmas, thereby controlling lava inundation potential. While several studies have addressed this behavior under faster cooling conditions, experimental data bridging the gap toward the quasi-equilibrium regime remain scarce due to the technical challenges of long-duration high-temperature rheometry experiments. This highlights the critical need for new datasets designed to quantify the rheological evolution pertinent to lava flow emplacement conditions. Here, we present a rheological dataset carried out on an Etnean trachybasalt, focusing on low cooling rates (0.1 and 0.5 °C/min) under variable shear strain rates (1–10 s⁻¹). Within the range of cooling and shear rates applied, results indicate that the cooling rate exerts a first-order control on crystallization kinetics, whereas the shear rate plays a secondary role, consistent with previous literature data. The technical validation is provided through instrument calibration and the verification of the chemical integrity of the pre- and post-run sample. Interestingly, the dataset captures the non-linear dependence of the crystallization onset temperature, which asymptotically approaches the thermodynamic liquidus (~1210 °C) as the cooling rate decreases. Beyond improving our understanding of magma crystallization kinetics, this dataset provides critical constraints for parameterizing the rheological evolution of lava flows during their emplacement in numerical models under varying thermal and dynamic regimes.

1. Background & Summary

Viscosity is a fundamental physical property that controls magma transport, chemical differentiation, and eruption dynamics (1-9). By regulating magma ascent rates, flow behavior within the crust and during lava emplacement, and the efficiency of gas segregation, viscosity ultimately dictates the style of volcanic eruptions (10-17). Magmas are frequently subjected to rapid changes in temperature and pressure, which promote disequilibrium crystallization, while they simultaneously experience variable shear strain rates during flow. In such magmas, the interplay among nano- to microlite crystallization under disequilibrium conditions, residual melt compositional and structural evolution primarily controls the macroscopic rheological behavior (3,15,18-30).

Several previous studies have shown that when mafic magmas are subjected to disequilibrium conditions that induce cooling and crystallization, the viscosity of the crystal-bearing suspension increases non-linearly, often by several orders of magnitude, fundamentally altering the capacity of the melt-crystal mixture to flow and its mechanical response to deformation (15,18,20,21,31,32). This pronounced reduction in the ability of magma to dissipate stress through viscous flow promotes the onset of non-Newtonian behavior, which can lead to a shift in the eruptive style during magma migration through the Earth's crust or affect the emplacement dynamics of a lava flow (6,13,16,33).

Consequently, there is a critical need for experimental data that quantify the transient rheological evolution of magma, while systematically accounting for the complex interplay between cooling rates (q), shear rates ($\dot{\gamma}$), and the resulting crystallization kinetics under disequilibrium conditions.

To address this, rotational rheometry, most commonly performed using a concentric cylinder (CC) geometry, represents one of the most suitable experimental approaches. This technique allows real-time monitoring of changes in the apparent viscosity (η_a) of the suspension in response to crystallization, which is tightly linked to the thermo-mechanical path experienced by the melt (3,21,28,34,35).

To explore the solidification of magma under disequilibrium conditions, the experimental strategy commonly adopted is the Cooling Deformation Experiment(s) (CDE) during which the melt is cooled at a constant cooling rate (q) and shear rate ($\dot{\gamma}$) pertinent to magma migration and lava flow emplacement dynamics (7,8,18,21,31,36,37). The interpretation of these rheological data allows us to better quantify the distinct roles of q and $\dot{\gamma}$ on the solidification paths of magmas. In addition, the parameterization and re-utilization of such data are essential for developing and calibrating more sophisticated numerical models that can accurately simulate magma ascent in conduit flow and lava emplacement scenarios (8,15,18,21).

Here, we present a dataset of rheological measurements from CDEs performed on a trachybasaltic lava from the 2001 Mt. Etna eruption. This dataset provides 6 new rheological measurements detailing the evolution of apparent viscosity as a function of temperature adopting two distinct cooling rates (0.1 and 0.5 °C/min) and three different shear rates (1, 5, and 10 s⁻¹). These data are intended to be reused by the community i) for understanding the concurrent role of cooling rate and shear rate on the solidification under disequilibrium kinetic conditions and ii) for parameterizing the rheological evolution of magma/lava flows and its timescales through more accurate numerical models.

2. Methods

2.1 Starting material, sample preparation, and chemical analysis

A trachybasaltic sample of lava from 2001 Mt. Etna eruption (³⁸) was utilized as starting material. Firstly, the rock sample was crushed and powdered using a jaw crusher and ring-mill. The resulting powder was then melted using a Fe-presaturated Pt crucible under air oxidizing conditions and ambient pressure in a Nabertherm® furnace at 1400 °C installed at the Experimental Volcanology and Petrology Laboratory (EVPLab) of the University of Roma Tre in Rome (Italy). In detail, the powdered sample was added to the crucible in batches of approximately 10-15 g every 10 minutes, to avoid the overflow of the melt due to foaming. When the crucible was completely filled, the melt was held to the target temperature of 1400 °C for approximately 2 hours to ensure the complete removal of bubbles and the melting of any pre-existing crystals. Subsequently, the melt was rapidly quenched in air to form a glass.

For the viscometry measurements, an aliquot of these glass chips was loaded and re-melted in a specific Fe-presaturated Pt₈₀Rh₂₀ cylindrical crucible with the following dimensions: 62 mm height, 32 mm inner diameter and 1.5 mm wall thickness. The chemical analysis was carried out using a Jeol JXA-iSP-100 electron probe microanalyzer (EPMA) equipped with five wavelength dispersive spectrometers at the High Pressures–High Temperatures Laboratory of Experimental Volcanology and Geophysics (HP-HT Lab) of the Istituto Nazionale di Geofisica e Vulcanologia (INGV) in Rome (Italy). In detail, the analyses were carried out on carbon-coated samples under high vacuum conditions, using an accelerating voltage of 15 kV and an electron beam current of 10nA, with a beam diameter of 5 µm. Elemental counting times were 10 s on the peak and 5 s on each of the two background positions. Corrections for interelemental effects were made using a ZAF (Z: atomic number; A: absorption; F: fluorescence) procedure. Calibration used a range of

standards from Micro-Analysis Consultants (MAC; <https://www.macstandards.co.uk>): albite (Si-PET, Al-TAP, Na-TAP), forsterite (Mg-TAP), augite (Fe-LIF), apatite (Ca-PET), orthoclase (K-PET), rutile (Ti-PET), rhodonite (Mn-LIF) and JEOL Cr metal (Cr-PET). To avoid alkali migration effects, Na and K were analyzed for first. BCR-2 was used as quality monitor standard during the analyses. Based on counting statistics, accuracy was better than 1–5%, except for elements with abundances below 1 wt%, for which accuracy was better than 5–10%. Precision was typically better than 1–5% for all analyzed elements. The chemical composition of the starting material is reported in **Table 1**.

2.2 Cooling Deformation Experiments (CDE)

Cooling Deformation Experiments (CDE) were carried out using a Concentric Cylinder (CC) apparatus at EVPLab. The CC apparatus includes a Rheotronic II Rotational Viscometer (Theta Instruments) with an Anton Paar Rheolab Qc viscometer head (full-scale torque of 75 mNm), a Fe-presaturated Pt₈₀Rh₂₀ cylindrical crucible (62, 32, and 1.5 mm in height, inner diameter, and wall thickness, respectively) and a Fe-presaturated Pt₈₀Rh₂₀ spindle (3.2 and 42 mm in diameter and length, respectively). The temperature of the sample was constantly monitored with a factory-calibrated S-type thermocouple (with a precision of $\pm 2^\circ\text{C}$) placed in close proximity to the crucible wall at the mid-height. In addition, the location of the thermocouple close to the sample permitted us to constantly monitor the absence of thermal lag in the sample during the experiments. The calibration of the CC apparatus was performed by using the standard glass NIST 717a (see *technical validation* section below).

For the CDE presented in this study the cooling rate (q) adopted are 0.1 and 0.5 $^\circ\text{C}/\text{min}$. For both q , a shear rate ($\dot{\gamma}$) of 1-5-10 s^{-1} are adopted. The range of q values reflects the thermal evolution typical of basaltic lava flows during emplacement and/or shallow transport, where

cooling is primarily governed by conductive heat loss (^{8,21}). The adopted $\dot{\gamma}$ values are likewise representative of mafic lava transport and emplacement, particularly in high-strain near-boundary and localized shear zones within advancing flows, where $\dot{\gamma}$ can locally approach the upper limit of our experimental range (^{8,15}). The CDE protocol begins with a *superliquidus* treatment aimed at fully homogenizing the melt. The sample is heated to a temperature of 1400 °C at a rate of 30 °C/min (⁷). When the temperature is reached, the melt is stirred at $\dot{\gamma}$ of 10 s⁻¹ approximately 3 hours, until a constant viscosity is recovered (within $\pm 3\%$ of the value related to the temperature). After this step, the experiment begins by applying to the melt a fixed q and $\dot{\gamma}$. The sampling frequency during each CDE is 60 seconds (s). The apparent viscosity (η_a) of the melt follows the viscosity-temperature path of the crystal-free melt at *superliquidus* temperatures (**Fig. 1**). In this study, the crystal-free melt viscosity (η_{liquid}) is modeled using the VFT equation (³⁹) as: $\text{Log } \eta_{liquid} = -A + [B/(T_k - C)]$, where T is the temperature in Kelvin. In detail, for this trachybasaltic melt the crystal-free melt viscosity was already measured in a previous work (⁷) and the VFT fit-parameters are reported in **Table 1**. Once the temperature decreases below the *liquidus*, the melt continues to follow the pure liquid over the incubation phase, until the crystallinity of the suspension is sufficient to influence the rheology of the system (**Fig. 1**).

To identify the temperature of crystallization onset (T_{onset}) during CDE, we adopt the point at which the measured viscosity deviates from the η_{liquid} of 10^{0.05} Pa s followed by a monotonic positive upward trend in viscosity. This viscosity increase reflects the development of a crystal fraction of ~1.8–3.3%, as estimated from empirical suspension models that incorporate shear rate and mean crystal aspect ratio (^{3,40}), for aspect ratios of 1–6 and $\dot{\gamma}$ of 0.1–10 s⁻¹. At this point, the viscosity diverges from the theoretical pure liquid trend and continues to increase until the achievement of the maximum stress of the device (i.e., 10⁵ Pa) during the experiment or manually

halted when a large viscosity drop is observed during measurement (**Fig. 1**). This behavior, termed viscous rupture, corresponds to ductile failure associated with pronounced shear localization within the crystal-bearing suspension (^{6,21,28}). After the interruption of the experiment, the experimental charge was reheated and the sample was again subjected to a *superliquidus* treatment before initiating another experimental run. The primary limitation of the CDE technique is related to post-experiment sampling. The combination of rapid crystallization kinetics and the high viscosities achieved makes it unfeasible to recover samples representative of the solidification history to which the melt was subjected, at best representing a snapshot of the final state (^{8,20,21}). This, in turn, hinders the chemical analysis of the residual melt or the textural characterization of the crystal population. At the end of the final experimental run, the crucible was emptied by remelting the sample at 1400 °C followed by rapid quenching. In addition, we evaluated the rheological impact of crystallization on the trachybasaltic melt from Mt. Etna using a normalized viscosity (η_x , ⁷). This value is derived by dividing the apparent viscosity (η_a) measured during CDE by the viscosity of the crystal-free liquid (i.e., $\eta_x = \eta_a / \eta_{liquid}$). It is important to clarify that the normalized viscosity is distinct from the relative viscosity (η_r), which is calculated as the ratio of apparent viscosity to residual melt viscosity. In fact, the calculation of η_r is unfeasible for CDE measurements as it requires data on the evolving composition of the residual melt to estimate the residual melt viscosity. Therefore, η_x is used as a comprehensive metric that reflects the combined influence of both physical factors (i.e., the presence of crystals) and chemical factors (i.e., the compositional evolution of the residual melt) on the suspension's rheology (^{16,21,37}).

3. Data Record

The data are available on Figshare at the following DOI: 10.6084/m9.figshare.30910934.

The dataset (⁴¹) consists of a single Microsoft Excel file named "raw_data.xlsx", which contains the complete time-series data from the Cooling Deformation Experiments (CDE). The file is organized into two main worksheets:

1. **Experimental Summary ("Summary")**: this worksheet provides a summary table of the experimental runs, listing the specific Cooling Rate and Shear Rate applied associated with the dataset.
2. **Experimental Data ("Raw_Data")**: this worksheet contains the raw rheological measurements. The data are organized in a side-by-side columnar format, where each experimental run is presented in a distinct block of columns grouped by the applied cooling rate (i.e., 0.1 or 0.5 °C/min) and shear rate (i.e., 1, 5 and 10 s⁻¹).

Variable Definitions

Within the "Raw_Data" worksheet, each CDE contains the following four variables:

- Temperature (°C): the temperature of the sample measured over time during the cooling ramp.
- Time (s): the duration of the experiment, with $t = 0$ corresponding to the start of the data acquisition at *superliquidus* conditions.
- Log Viscosity (Pa s): the base-10 logarithm of the measured apparent viscosity (η_a) of the suspension.
- Log Normalized Viscosity: the base-10 logarithm of the normalized viscosity (η_x), calculated as described in "2.2 Cooling Deformation Experiments (CDE)" section.

4. Technical Validation

4.1 Instrument Calibrations

The Concentric Cylinder (CC) apparatus was technically validated to ensure the accuracy of both viscosity and temperature measurements. Prior to calibrating the rheometer, we characterized the furnace to identify a stable hot zone, ensuring the experiments were free from appreciable thermal gradients (see ^{7,16} for additional information). The CC apparatus was calibrated using the NIST 717a standard reference material, a borosilicate glass with Newtonian properties ($n = 1.0$). Calibration measurements were performed across a temperature interval of 896 to 1504 °C, covering a torque range of ~0.1 to ~70.0 mN m and resulting in a viscosity range between $\sim 10^{1.1}$ to $\sim 10^{4.6}$ Pa s, using shear rates ranging from 1 to 10 s⁻¹ (see ^{7,16} for additional information). As previously mentioned, the placement of the S-type thermocouple in close proximity to the sample allowed for constant monitoring to verify the absence of thermal lag throughout the sample during CDE experiments. In detail, no thermal lag was observed within the system, ensuring reliable temperature control across the entire experimental range up to a q of 10 °C/min.

4.2 Sample Chemical Integrity

A primary element in validating the CDE measurements was verifying that no chemical modification occurred in the trachybasaltic sample. EPMA analyses conducted before and after the experiments confirmed the chemical stability of the material. Firstly, we ensured that the chemical composition of the starting glass (**Table 1**) was consistent with previously published analyses for the 2001 Mt. Etna lava (⁷), confirming that the prepared material was representative of the target composition. In addition, at the conclusion of the final CDE run, the experimental charge was remelted at 1400 °C, subjected to a final *superliquidus* treatment cycle, and then rapidly quenched. EPMA analyses performed on the resulting glass chips showed no significant alkali loss (Na and K) despite the high-temperature and long-duration experimental steps (**Table 1**).

4.3 Results and Data Consistency

The viscosity data related to the CDE measurements carried out at different cooling rate (q) and shear rate ($\dot{\gamma}$) are reported as a function of temperature (T) in **Fig. 2** and **Fig. 3**. At *superliquidus* T , the apparent viscosity (η_a) increases with decreasing T in all experiments. For CDE carried out at $\dot{\gamma}$ of 1 s^{-1} a noisy η_a signal is observed between 1400 and 1300 °C. This effect is attributable to the low torque recorded by the measuring system, resulting from the coupled effect of low $\dot{\gamma}$ and low η_a of the crystal-free melt at high T . Below 1300-1250 °C, once sufficient torque is reached for each $\dot{\gamma}$, in all CDE the viscosity increase trends are consistent with the evolution of the crystal-free melt viscosity modeled with the VFT equation, using the parameter reported in **Table 1**.

The temperature at which the crystallization takes place (T_{onset}) was not chosen arbitrarily but was operationally defined as the point at which the measured η_a shows a deviation of $10^{0.05}$ Pa s from the modeled crystal-free melt viscosity (see Methods Section 2.2). All T_{onset} retrieved following this approach (see **Table 2**) are lower than 1210 °C that represents the *liquidus* temperature estimation of the starting chemical composition determined through the MELTS code⁽⁴²⁾ in **Di Fiore et al. (2022)**⁷. The observed T_{onset} show higher values with decreasing q and increasing $\dot{\gamma}$. Notably, the experiment conducted at $q = 0.5$ °C/min and $\dot{\gamma}$ of 5 s^{-1} displays a non-monotonic rheological evolution (**Fig. 2**), characterized by a transient decrease in apparent viscosity (η_a ; up to ~ 0.2 log units). During this interval, the viscosity signal becomes noticeably noisier than during the rest of the experiment, within a temperature range of 1125–1100 °C. After this phase, viscosity increases rapidly, culminating in a large viscosity drop indicative of viscous rupture. Similarly, the experiment performed at $q = 0.5$ °C/min and $\dot{\gamma}$ of 10 s^{-1} exhibits a temperature interval between 1130 and 1110 °C characterized by a marked increase in viscosity

signal noise, followed by a sharp viscosity increase. The occurrence of these comparable noisy intervals suggests that the observed rheological instability is likely related to shear-induced self-organization (^{43–45}), where high-aspect-ratio crystalline phases such as plagioclase tend to align with the flow direction (^{3,46–48}). Finally, consistent with the trend observed for T_{onset} , the interruption of the experiments caused by the onset of viscous rupture (^{6,15,21}) also occurs at progressively lower T (from 1140 to 1077 °C **Table 2**) as q increases and $\dot{\gamma}$ decreases. The only exception is the experiment conducted at q of 0.5 °C/min and $\dot{\gamma}$ of 1 s⁻¹, in which no viscous rupture was observed in the η_a interval accessible with our CC setup. In this case, the experiment was interrupted when the torque limit of the CC was achieved. The trends observed for both crystallization onset and viscous rupture are consistent with previously published rheological evolution patterns for similar mafic magmas subjected to comparable disequilibrium kinetic conditions in terms of q and $\dot{\gamma}$ (^{6,7,15,16,20,21,31,36}).

Finally, the normalized viscosities (η_x) of the CDE, plotted as a function of T in **Fig. 3** highlight the impact of crystallization during the solidification of the Etnean trachybasalt under different disequilibrium conditions. The η_x values show a clear dependence on the experimental parameters, particularly, the onset of viscous rupture occurs at higher T and lower η_x values with decreasing q and increasing $\dot{\gamma}$. This behavior is consistent with previous findings reported in the literature (^{6,15,21,37}).

4.4 Modeling the crystallization kinetics

To assess the physical validity and consistency of the low- q experimental dataset presented in this study, we integrated our crystallization onset temperature (T_{onset}) results with data previously reported by **Di Fiore et al. (2022)**⁷, in which higher q (from 1 to 5 °C/min) were investigated within the same $\dot{\gamma}$ range (from 1 to 10 s⁻¹), adopting the same CC setup and geometries

utilized in this study. The T_{onset} values corresponding to each q (and same $\dot{\gamma}$) were fitted using a global regression model based on the Lasocka relationship⁽⁴⁹⁾ as follows:

$$T_{onset} = a - b \times \ln \ln q \quad \text{Eq. 1}$$

where a and b are fitting parameters (**Fig. 4**, respective values of a and b for each $\dot{\gamma}$ are listed in **Table 2**). The coefficients of determination (R^2) for the fittings yield values \geq of 0.94 (**Table 3**). Although **Eq. 1** was originally developed to describe the rate-dependence of the glass transition temperature, this semi-empirical logarithmic relationship is widely used to model non-isothermal crystallization kinetics⁽⁵⁰⁻⁵²⁾, as both transformations are governed by time-dependent, thermally activated mechanisms.

The observed trends, and specifically the kinetic delay of crystallization with increasing q and, conversely, the increase of T_{onset} with increasing $\dot{\gamma}$, are in excellent agreement with previous experimental studies on silicate melts carried out under similar experimental conditions^(6,7,15,16,20,21,31,36). In addition, extending the investigated range of q to values < 1 °C/min in this study, allows us to observe and quantify the non-linear dependence of T_{onset} for this silicate melt composition. In detail, with decreasing q , T_{onset} progressively approaches the *liquidus* temperature of 1210 °C, previously estimated in **Di Fiore et al. (2022)**⁷ on a thermodynamic basis through the MELTS code⁽⁴²⁾. It is important to consider that while the rheological determination of the crystallization onset is subject to inherent experimental uncertainties related to the definition of the viscosity departure point, the coherence of the integrated fit across different dynamic conditions confirms the reliability of CDE measurements presented in this study and of the crystallization onset detection method.

Acknowledgements

F.D.F. acknowledges funding from the MUR (Ministero dell'Università e della Ricerca) PNRR Project “Monitoring Earth Evolution and Tectonics” (MEET, Grant #D53C22001400005).

F.D.F. received additional support from INGV – Progetti Ricerca Libera: PANTA REI. AV acknowledges funding by MUR PRIN Project P20222BP7J.

Code availability

No custom code was used to generate or process the data described in the manuscript.

Competing interests

The authors declare no competing interests.

Contributions

F.D.F.: Conceptualization – Methodology – Validation - Formal Analysis – Investigation – Data Curation – Writing-Original Draft – Review & Editing – Visualization. A.V.: Methodology – Validation – Review & Editing – Visualization – Resources – Funding Acquisition.

Data Availability

The data are available on Figshare at the following DOI: [10.6084/m9.figshare.30910934](https://doi.org/10.6084/m9.figshare.30910934)

Figures

Figure 1 Schematic representation of the rheological path during a Cooling Deformation Experiment (CDE) (modified from ⁶). The grey shaded area represents the *superliquidus* field. Upon cooling below the *liquidus* temperature, the system enters in the nucleation incubation zone. The onset of crystallization corresponds to the deviation of the measured apparent viscosity (solid line) from the theoretical pure liquid trend (dashed line). The experiment continues until the instrument torque limit is reached or viscous rupture occurs.

Figure 2 Evolution of apparent viscosity (η_a) as a function of temperature (T). The plots show the CDE results for the trachybasaltic melt cooled at rates (q) of 0.1 and 0.5 °C/min, under shear rates ($\dot{\gamma}$) of 1, 5, and 10 s⁻¹. The solid line represents the measured data, while the thin black line indicates the theoretical viscosity of the crystal-free melt (η_{liquid}) modeled using the VFT equation (parameters in **Table 1**).

Figure 3 Evolution of normalized viscosity (η_x) as a function of temperature (T). The η_x is calculated as the ratio between the measured apparent viscosity (η_a) and the calculated pure liquid viscosity (η_{liquid}). The curves highlight the rheological impact of crystallization under different disequilibrium conditions. Higher shear rates ($\dot{\gamma}$) and lower cooling rates (q) shift the viscosity increase to higher temperatures.

Figure 4 Crystallization onset modeling. (a) Crystallization onset temperatures (T_{onset}) plotted as a function of cooling rate (q) for different shear rates ($\dot{\gamma} = 1, 5, 10$ s⁻¹). Symbols represent the experimental data from this study (low- q represented by the shaded grey field) integrated with high- q data from **Di Fiore et al. (2022)**⁷. Dashed lines represent the global regression fit based on the Lasocka relationship ($T_{onset} = a - b \times \ln q$; ⁴⁹). The red circle indicates the thermodynamic liquidus temperature (~1210 °C) estimated through the MELTS code (⁴²).

References

1. Parfitt, E. A. A discussion of the mechanisms of explosive basaltic eruptions. *Journal of Volcanology and Geothermal Research* **134**, 77–107 (2004).
2. Giordano, D., Russell, J. K. & Dingwell, D. B. Viscosity of magmatic liquids: A model. *Earth Planet. Sci. Lett.* **271**, 123–134 (2008).
3. Vona, A., Romano, C., Dingwell, D. B. & Giordano, D. The rheology of crystal-bearing basaltic magmas from Stromboli and Etna. *Geochim. Cosmochim. Acta* **75**, 3214–3236 (2011).
4. Gonnermann, H. M. Magma Fragmentation. *Annu. Rev. Earth Planet. Sci.* **43**, 431–458 (2015).
5. Calabrò, L., Esposti Ongaro, T., Giordano, G. & de' Michieli Vitturi, M. Reconstructing Pyroclastic Currents' Source and Flow Parameters From Deposit Characteristics and Numerical Modeling: The Pozzolane Rosse Ignimbrite Case Study (Colli Albani, Italy). *J. Geophys. Res. Solid Earth* **127**, e2021JB023637 (2022).
6. Di Fiore, F., Vona, A., Kolzenburg, S., Mollo, S. & Romano, C. An Extended Rheological Map of Pāhoehoe—‘A‘ā Transition. *J. Geophys. Res. Solid Earth* **126**, e2021JB022035 (2021).
7. Di Fiore, F., Vona, A., Costa, A., Mollo, S. & Romano, C. Quantifying the influence of cooling and shear rate on the disequilibrium rheology of a trachybasaltic melt from Mt. Etna. *Earth Planet. Sci. Lett.* **594**, 117725 (2022).
8. Kolzenburg, S., Chevrel, M. O. & Dingwell, D. B. Magma / Suspension Rheology. *Rev. Mineral. Geochem.* **87**, 639–720 (2022).
9. Valdivia, P. *et al.* Nanoscale chemical heterogeneities control the viscosity of andesitic magmas. *Commun. Earth Environ.* **6**, 455 (2025).
10. Gonnermann, Helge. M. *et al.* Permeability During Magma Expansion and Compaction. *J. Geophys. Res. Solid Earth* **122**, 9825–9848 (2017).
11. Moitra, P., Gonnermann, H. M., Houghton, B. F. & Tiwary, C. S. Fragmentation and Plinian eruption of crystallizing basaltic magma. *Earth Planet. Sci. Lett.* **500**, 97–104 (2018).
12. Polacci, M. *et al.* Crystallisation in basaltic magmas revealed via in situ 4D synchrotron X-ray microtomography. *Sci. Rep.* **8**, 8377 (2018).

13. Arzilli, F. *et al.* Magma fragmentation in highly explosive basaltic eruptions induced by rapid crystallization. *Nat. Geosci.* **12**, 1023–1028 (2019).
14. Scarani, A. *et al.* A chemical threshold controls nanocrystallization and degassing behaviour in basalt magmas. *Commun. Earth Environ.* **3**, 284 (2022).
15. Di Fiore, F. *et al.* Experimental Constraints on the Rheology of Lavas From 2021 Cumbre Vieja Eruption (La Palma, Spain). *Geophys. Res. Lett.* **50**, e2022GL100970 (2023).
16. Di Fiore, F. *et al.* Magma titanium and iron contents dictate crystallization timescales and rheological behaviour in basaltic volcanic systems. *Commun. Earth Environ.* **5**, 283 (2024).
17. Cassetta, M. *et al.* Chemically Driven Nano-Elastic Heterogeneities Control Fragility in Volcanic Melts. *Advanced Science* **n/a**, e12063 (2025).
18. Giordano, D. *et al.* Thermo-rheological magma control on the impact of highly fluid lava flows at Mt. Nyiragongo. *Geophys. Res. Lett.* **34**, (2007).
19. Sehlke, A. *et al.* Pahoehoe to `a`a transition of Hawaiian lavas: an experimental study. *Bull. Volcanol.* **76**, 876 (2014).
20. Kolzenburg, S., Giordano, D., Cimarelli, C. & Dingwell, D. B. In situ thermal characterization of cooling/crystallizing lavas during rheology measurements and implications for lava flow emplacement. *Geochim. Cosmochim. Acta* **195**, 244–258 (2016).
21. Di Fiore, F. *et al.* Impact of cooling rate on rheology and emplacement dynamics of basaltic lavas: Insights from the January 2024 Sundhnúksíggar eruption (Iceland). *Journal of Volcanology and Geothermal Research* **466**, 108400 (2025).
22. Giuliani, G. *et al.* The rheological evolution of a phonotephritic melt upon variable degrees of carbonate assimilation and deformation regimes. *Chem. Geol.* **680**, 122711 (2025).
23. Di Genova, D. *et al.* In situ observation of nanolite growth in volcanic melt: A driving force for explosive eruptions. *Sci. Adv.* **6**, eabb0413 (2020).
24. Cassetta, M. *et al.* Effect of the alkali vs iron ratio on glass transition temperature and vibrational properties of synthetic basalt-like glasses. *Spectrochim. Acta A Mol. Biomol. Spectrosc.* **293**, 122430 (2023).
25. Cassetta, M. *et al.* Nanolite cargo evolution in trachybasaltic glass comparing magnetite and augite. *Sci. Rep.* **15**, 39170 (2025).
26. Szewczyk, D. & Cassetta, M. Colossal low-temperature upturn in the heat capacity of volcanic glasses. *J. Non. Cryst. Solids* **637**, 123046 (2024).

27. Giuliani, G. *et al.* The effect of carbonate assimilation and nanoheterogeneities on the viscosity of phonotephritic melt from Vesuvius. *Chem. Geol.* **670**, 122408 (2024).
28. Di Fiore, F. *et al.* Experimental insights on the shear-induced crystallization of a phonotephrite magma. *Chem. Geol.* **637**, 121682 (2023).
29. Di Fiore, F. *et al.* Kinetic partitioning of major and trace cations between clinopyroxene and phonotephritic melt under convective stirring conditions: New insights into clinopyroxene sector zoning and concentric zoning. *Chem. Geol.* **584**, 120531 (2021).
30. Zandonà, A. *et al.* Non-stoichiometric crystal nucleation in a spodumene glass containing TiO₂ as seed former: Effects on the viscosity of the residual melt. *J. Non. Cryst. Solids* **619**, 122563 (2023).
31. Kolzenburg, S., Di Genova, D., Giordano, D., Hess, K. U. & Dingwell, D. B. The effect of oxygen fugacity on the rheological evolution of crystallizing basaltic melts. *Earth Planet. Sci. Lett.* **487**, 21–32 (2018).
32. Haag, V., Höskuldsson, Á. & Soldati, A. Constraining the high-temperature viscoelastic behavior of basaltic melts through oscillatory rheometry. *Chem. Geol.* **695**, 123030 (2025).
33. Dingwell, D. B. Volcanic Dilemma--Flow or Blow? *Science* (1979). **273**, 1054–1055 (1996).
34. Spera, F. J., Borgia, A., Strimple, J. & Feigenson, M. Rheology of melts and magmatic suspensions: 1. Design and calibration of concentric cylinder viscometer with application to rhyolitic magma. *J. Geophys. Res. Solid Earth* **93**, 10273–10294 (1988).
35. Sato, H. Viscosity measurement of subliquidus magmas: 1707 basalt of Fuji volcano. *Journal of Mineralogical and Petrological Sciences* **100**, 133–142 (2005).
36. Harris, M. A., Kolzenburg, S. & Chevrel, M. O. The viscosity of multiphase lava: New insights from integrating laboratory and field measurements. *Earth Planet. Sci. Lett.* **671**, 119642 (2025).
37. Recchuiti, E. M., Höskuldsson, Á. & Soldati, A. Disequilibrium rheology of basaltic magma: Cooling deformation experiments with one-step and two-step cooling rates. *Journal of Volcanology and Geothermal Research* **465**, 108364 (2025).
38. Behncke, B. & Neri, M. The July/August 2001 eruption of Mt. Etna (Sicily). *Bull. Volcanol.* **65**, 461–476 (2003).
39. Tammann, G. & Hesse, W. Die Abhängigkeit der Viscosität von der Temperatur bei unterkühlten Flüssigkeiten. *Z. Anorg. Allg. Chem.* **156**, 245–257 (1926).

40. Mader, H. M., Llewellyn, E. W. & Mueller, S. P. The rheology of two-phase magmas: A review and analysis. *Journal of Volcanology and Geothermal Research* **257**, 135–158 (2013).
41. Di Fiore, F. V. A. Raw Data from from Concentric Cylinder Measurements (Di Fiore and Vona). *FigShare* - <https://doi.org/10.6084/m9.figshare.30910934> (2026).
42. Ghiorso, M. S. & Sack, R. O. Chemical mass transfer in magmatic processes IV. A revised and internally consistent thermodynamic model for the interpolation and extrapolation of liquid-solid equilibria in magmatic systems at elevated temperatures and pressures. *Contributions to Mineralogy and Petrology* **119**, 197–212 (1995).
43. Kirkwood, D. H., Suéry, M., Kapranos, P., Atkinson, H. V & Young, K. P. *Semi-Solid Processing of Alloys*. <http://www.springer.com/series/856>.
44. Gwalani, B. *et al.* Extreme shear-deformation-induced modification of defect structures and hierarchical microstructure in an Al–Si alloy. *Commun. Mater.* **1**, 85 (2020).
45. Ji, S., Wang, K. & Dong, X. An Overview on the Process Development and the Formation of Non-Dendritic Microstructure in Semi-Solid Processing of Metallic Materials. *Crystals* vol. 12 Preprint at <https://doi.org/10.3390/cryst12081044> (2022).
46. Ishibashi, H. & Sato, H. Viscosity measurements of subliquidus magmas: Alkali olivine basalt from the Higashi-Matsuura district, Southwest Japan. *Journal of Volcanology and Geothermal Research* **160**, 223–238 (2007).
47. Cimarelli, C., Costa, A., Mueller, S. & Mader, H. M. Rheology of magmas with bimodal crystal size and shape distributions: Insights from analog experiments. *Geochemistry, Geophysics, Geosystems* **12**, (2011).
48. Mollo, S. *et al.* Thermodynamics and kinetics of cation partitioning between plagioclase and trachybasaltic melt in static and dynamic systems: A reassessment of the lattice strain and electrostatic energies of substitution. *Geochim. Cosmochim. Acta* **384**, 27–43 (2024).
49. Lasocka, M. The effect of scanning rate on glass transition temperature of splat-cooled Te₈₅Ge₁₅. *Materials Science and Engineering* **23**, 173–177 (1976).
50. Kuo, P.-H. & Du, J. Crystallization behavior of Li_{1+x}Al_xGe_{2-x}(PO₄)₃ glass-ceramics: Effect of composition and thermal treatment. *J. Non. Cryst. Solids* **525**, 119680 (2019).
51. Ahmad, M. *et al.* Physical characterization and crystallization kinetics of amorphous BiSe chalcogenide glasses. *Journal of Materials Research and Technology* **16**, 1114–1121 (2022).

52. Khan, S. *et al.* Luminescence, mechanical and non-isothermal crystallization kinetics properties of MnO-doped borosilicate glasses for photonics applications. *J. Solid State Chem.* **353**, 125608 (2026).

ARTICLE IN PRESS

Table 1 Chemical composition of starting material and post-run glasses. Data are reported in wt.% and correspond to the average of 10 analyses. The VFT fitting parameters are also reported from Di Fiore *et al.* (2022)⁷.

Oxide	<i>Starting Material</i>		<i>Post CDE runs</i>	
	wt. %	s.d.	wt. %	s.d.
SiO ₂	47.39	0.24	47.51	0.28
TiO ₂	1.63	0.03	1.64	0.05
Al ₂ O ₃	16.58	0.20	16.64	0.22
FeO	10.38	0.18	10.29	0.19

MnO	0.17	0.01	0.17	0.02
MgO	6.30	0.08	6.33	0.09
CaO	10.99	0.00	10.92	0.23
Na ₂ O	3.32	0.21	3.25	0.07
K ₂ O	1.90	0.06	1.84	0.05
P ₂ O ₅	0.46	0.02	0.48	0.03

<i>VFT parameters</i>	<i>A</i>	<i>B</i>	<i>C</i>
	-5.1	6321	553.2

Table 2 Results from Cooling Deformation Experiments (CDE).

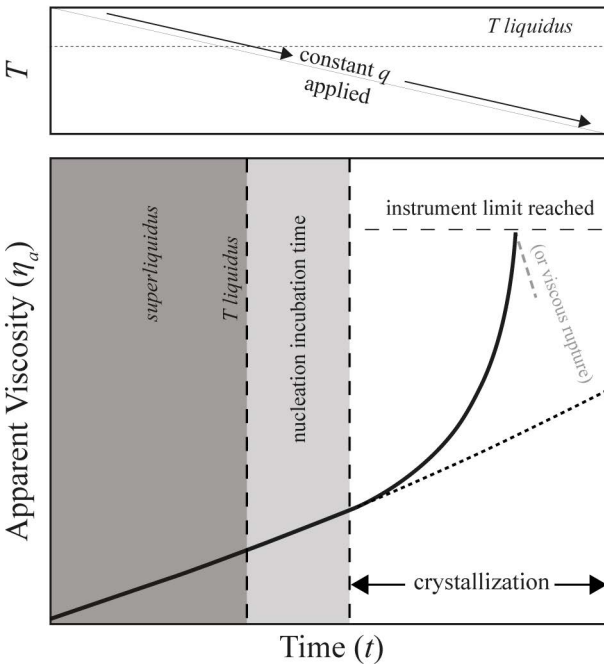
<i>q</i>	$\dot{\gamma}$	<i>T_{onset}</i>	<i>T_{end}</i>	η_a	η_x
°C/min	s ⁻¹	°C	°C	Log (Pa s)	Log units
0.1	1	1181	1087	4.30	1.56
0.5	1	1146	1055	4.86	1.91
0.1	5	1201	1140	3.29	1.01
0.5	5	1163	1077	4.20	1.37
0.1	10	1203	1143	2.99	0.81
0.5	10	1179	1088	3.73	1.01

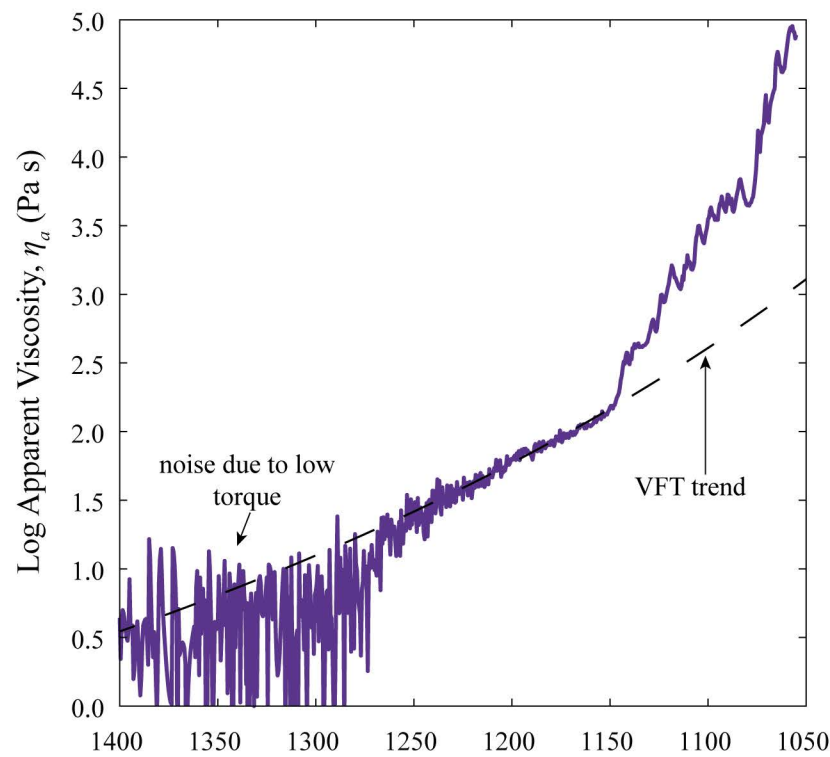
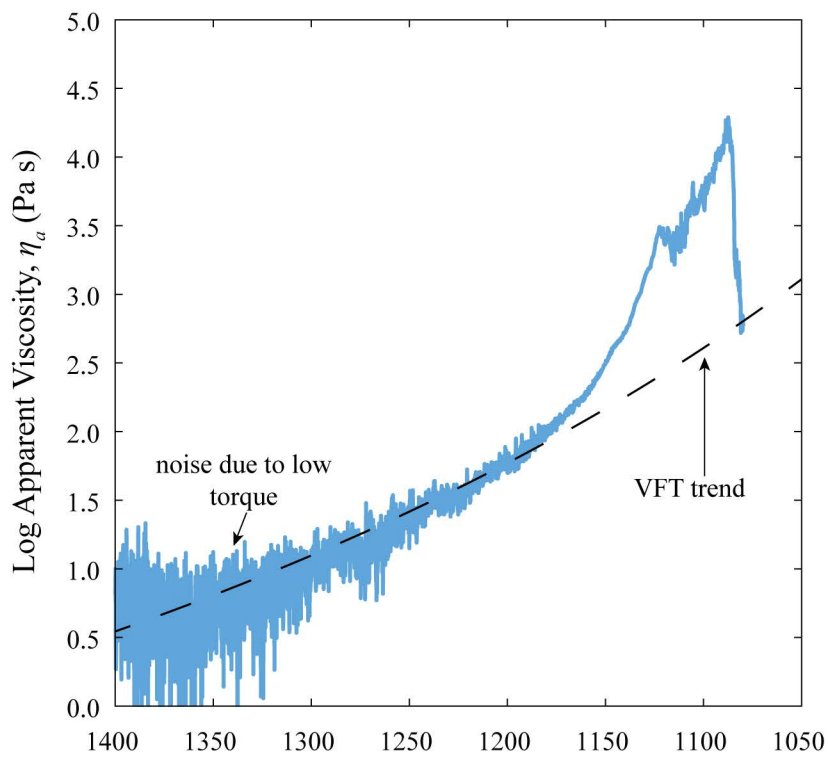
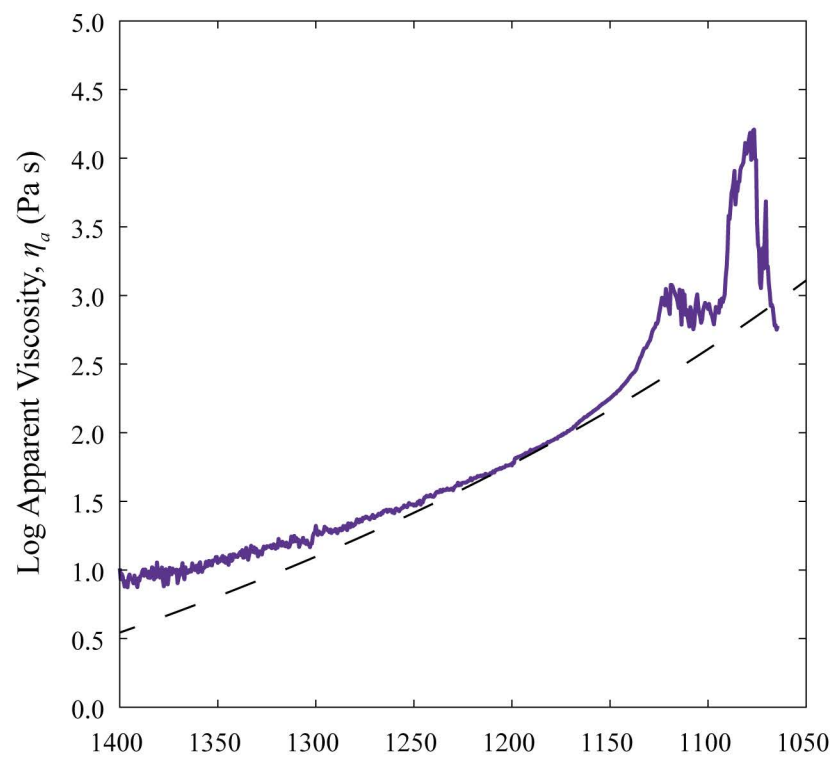
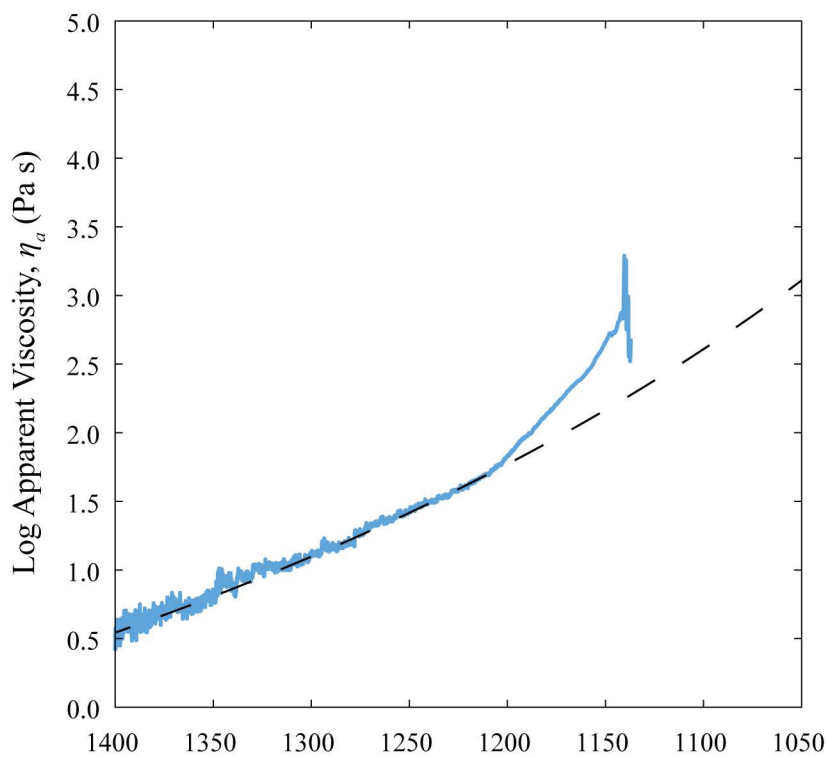
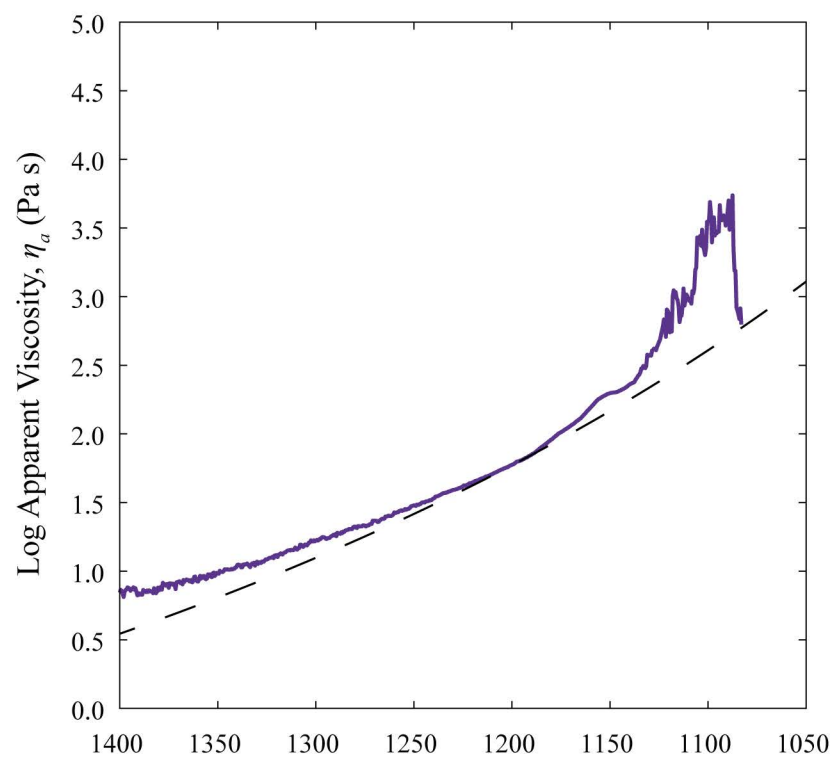
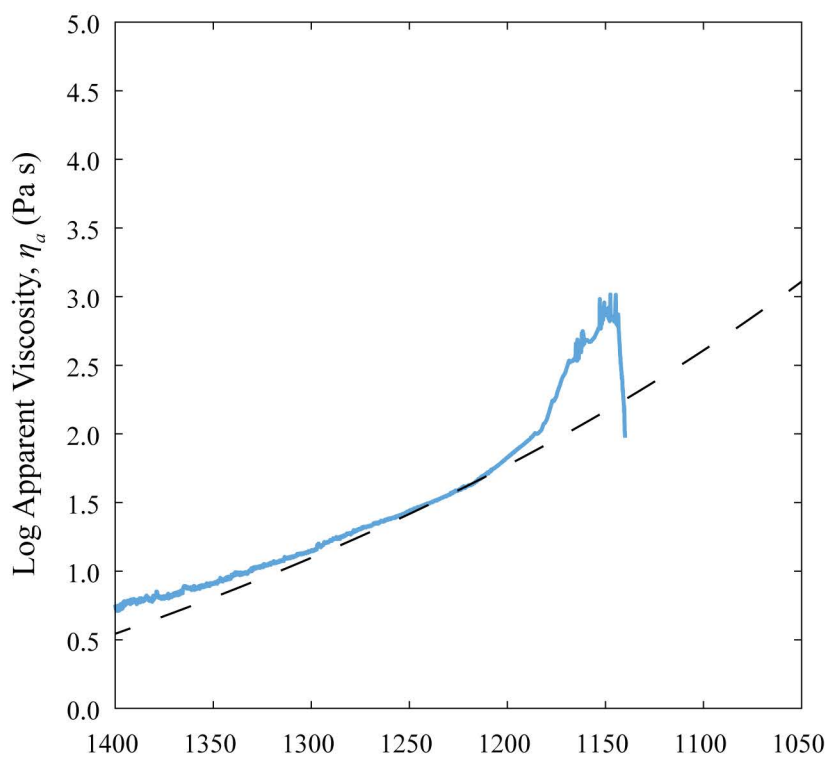
Table 3 Summary of the fitting parameters (a, b) and determination coefficients (R^2) for the Lasocka relationship describing the crystallization onset temperature (T_{onset}). The fit was carried out on the integrated dataset comprising T_{onset} values from this work and from **Di Fiore et al. (2022)**⁷.

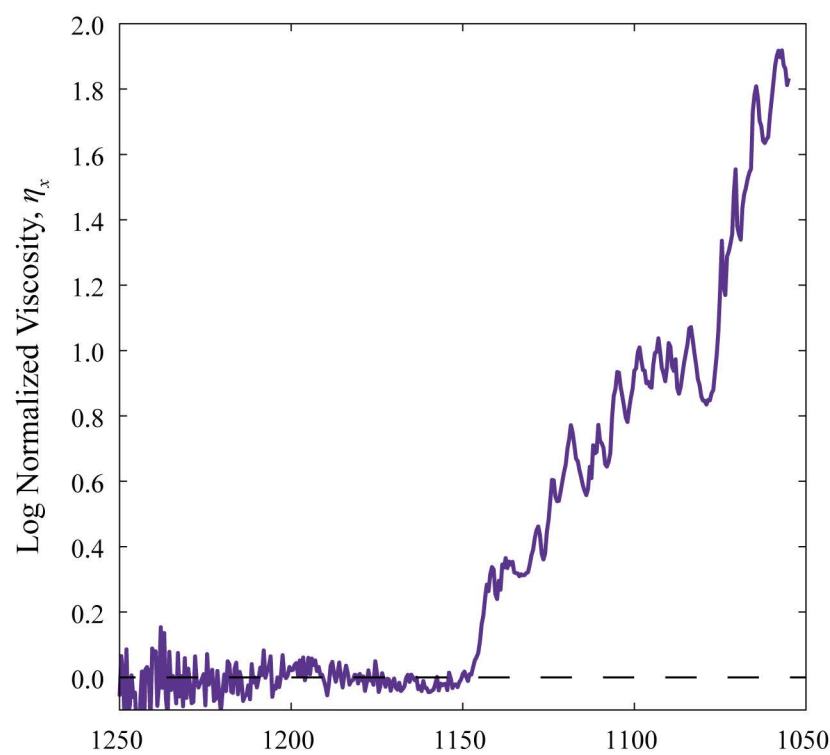
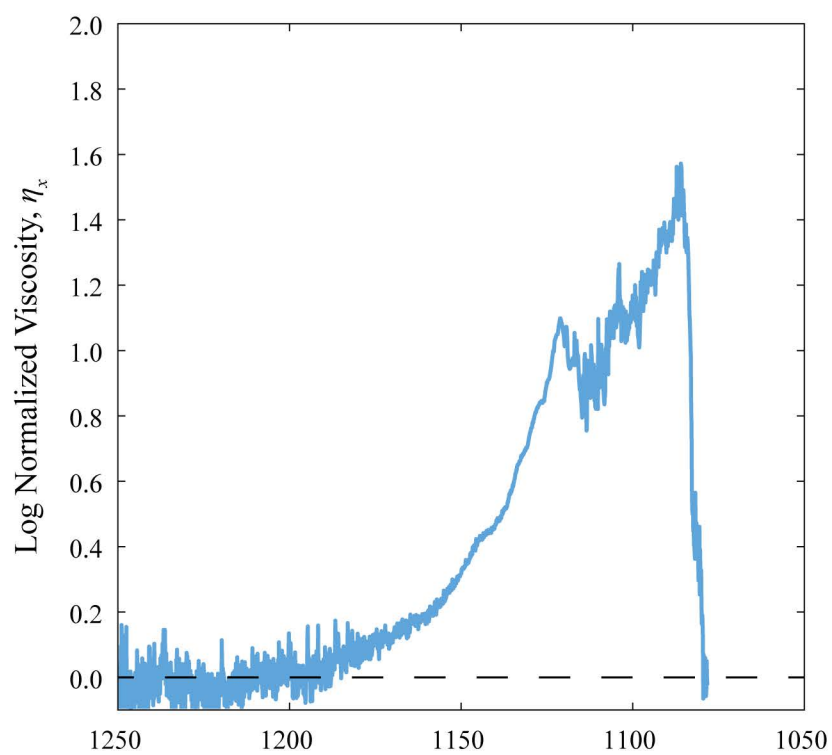
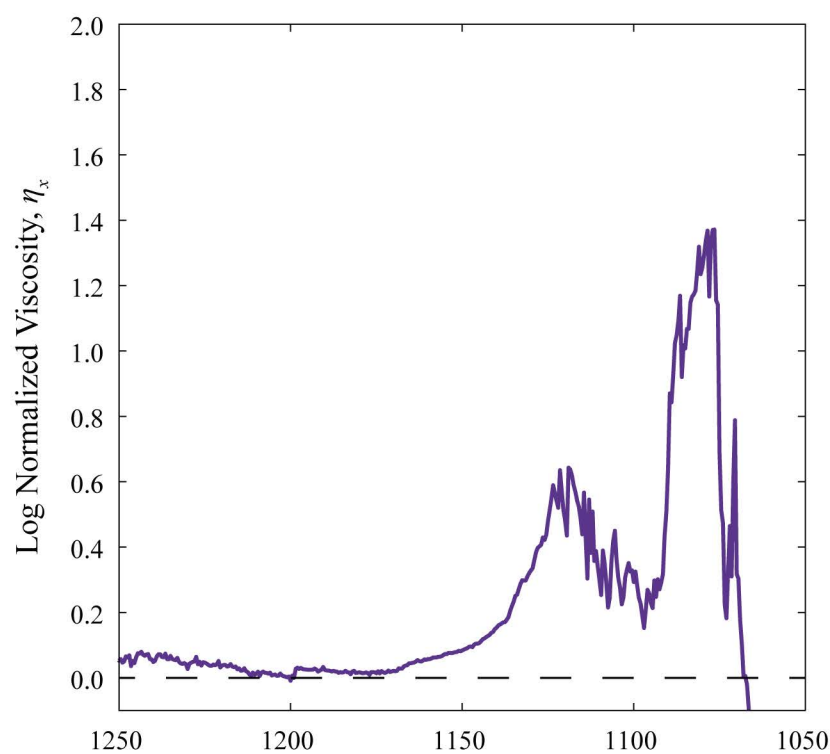
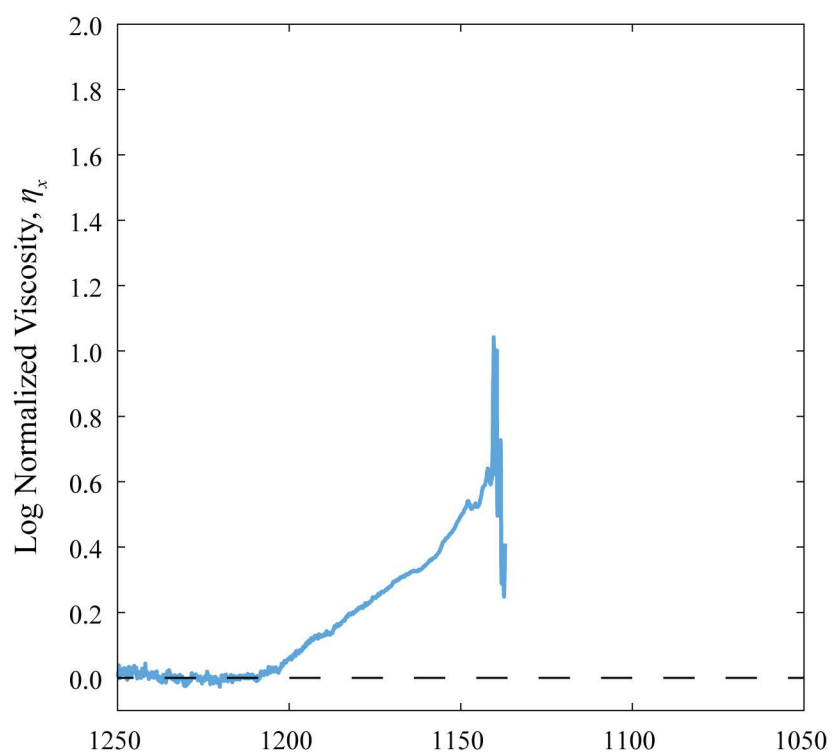
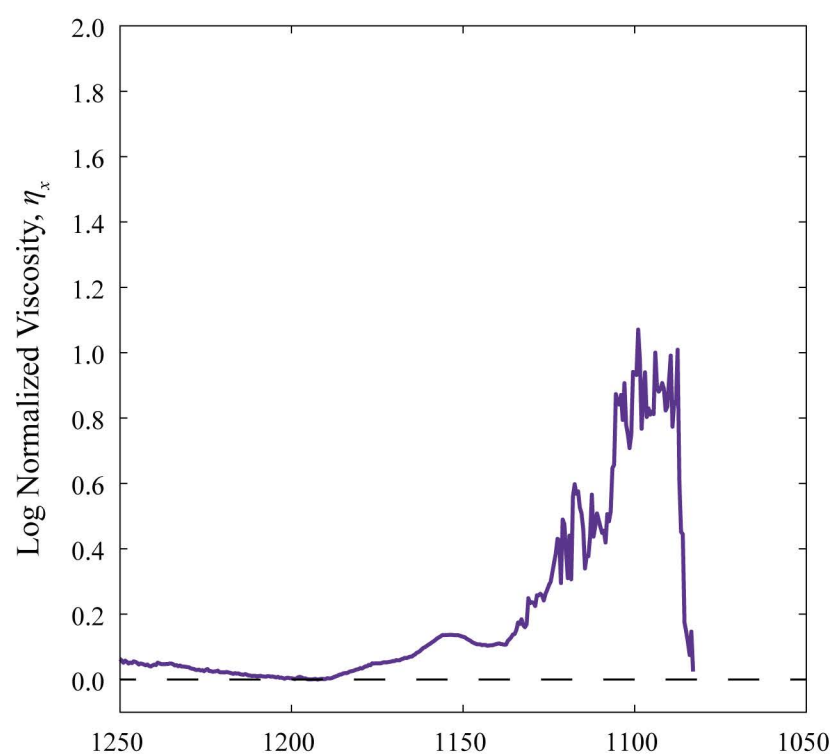
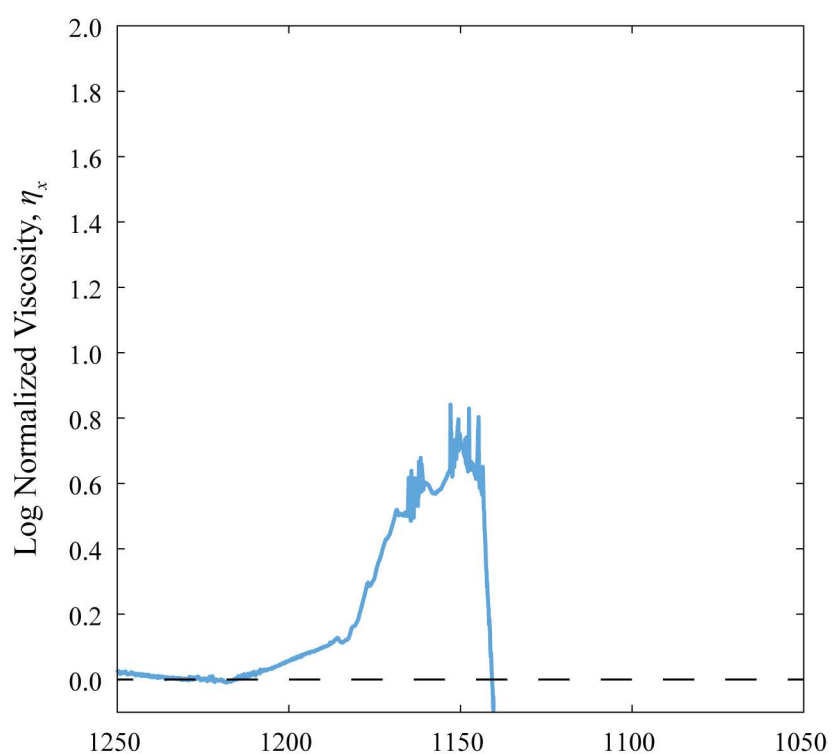
<i>q</i>	$\dot{\gamma}$	<i>Fit Parameters</i>		R^2
°C/min	s ⁻¹	<i>a</i>	<i>b</i>	-
0.1	1	1137.1	-19.267	0.95
0.5	1			
0.1	5	1151.4	-21.546	0.98
0.5	5			
0.1	10	1167.6	-16.874	0.94
0.5	10			

ARTICLE IN PRESS

Cooling Deformation Experiment



Cooling rate (q) = 0.1 °C/minCooling rate (q) = 0.5 °C/minShear rate ($\dot{\gamma}$) = 1 s⁻¹Shear rate ($\dot{\gamma}$) = 5 s⁻¹Shear rate ($\dot{\gamma}$) = 10 s⁻¹Temperature, T (°C)Temperature, T (°C)

Cooling rate (q) = 0.1 °C/minCooling rate (q) = 0.5 °C/minShear rate ($\dot{\gamma}$) = 1 s⁻¹Shear rate ($\dot{\gamma}$) = 5 s⁻¹Shear rate ($\dot{\gamma}$) = 10 s⁻¹Temperature, T (°C)Temperature, T (°C)

